PAPER

Check for updates

Crack patterns of drying dense bacterial suspensions†

Xiaolei Ma, [iD] *[a] Zhengyang Liu,[a] Wei Zeng,[ab] Tianyi Lin,[a] Xin Tian[c] and Xiang Cheng [iD] *[a]

Drying of bacterial suspensions is frequently encountered in a plethora of natural and engineering processes. However, the evaporation-driven mechanical instabilities of dense consolidating bacterial suspensions have not been explored heretofore. Here, we report the formation of two different crack patterns of drying suspensions of *Escherichia coli* (*E. coli*) with distinct motile behaviors. Circular cracks are observed for wild-type *E. coli* with active swimming, whereas spiral-like cracks form for immotile bacteria. Using the elastic fracture mechanics and the poroelastic theory, we show that the formation of the circular cracks is determined by the tensile nature of the radial drying stress once the cracks are initiated by the local order structure of bacteria due to their collective swimming. Our study demonstrates the link between the microscopic swimming behaviors of individual bacteria and the mechanical instabilities and macroscopic pattern formation of drying bacterial films. The results shed light on the dynamics of active matter in a drying process and provide useful information for understanding various biological processes associated with drying bacterial suspensions.

1 Introduction

Active matter is a class of nonequilibrium systems consisting of autonomous units that convert local internal or ambient free energy into mechanical motions. A large number of biological and physical systems including suspensions of a self-propelled cytoskeleton,[1,2] swarms of bacteria[3–5] and clusters of synthetic active colloids[6–8] can be categorized as active matter, which exhibit fascinating statistical and mechanical properties that have drawn tremendous attention in recent years due to their fundamental and technical interests.[9–11] While extensive studies have been conducted to understand the emergent collective dynamics of active matter in fluid states,[12,13] it is still unclear whether and how the local activity affects the macroscopic mechanical properties of consolidating active matter during a drying process.

Drying of bacterial suspensions as a premier model of active matter plays a crucial role in many biological, environmental and industrial processes and influences diverse phenomena ranging from biofilm formation,[14] spreading of disease[15] and food hygiene[16] to interbacterial competition for survival,[17] coating and self-assembly.[18–20] The active swimming of bacteria can profoundly modify the complex interplays between solid, liquid and vapor phases as a suspension passes from a fluid to a solid state during drying, giving rise to the unusual growth dynamics and morphologies of "coffee rings" in dried deposits.[18–22] However, these existing studies are all limited to the dilute limit of bacterial suspensions, where bacteria are deposited near the edge of drying drops. The mechanical instabilities of thick consolidating bacterial films formed by drying dense bacterial suspensions remain elusive, despite the fact that such instabilities and the resulting crack patterns have been extensively investigated in counterpart passive particle systems.[23–32]

Here, we explored the effect of bacterial swimming on the mechanical instabilities and desiccation crack patterns of dense consolidating bacterial suspensions. We used a wild-type strain of *Escherichia coli* (*E. coli*) as our model bacteria, which display the classic run-and-tumble swimming in water.[33] As a control, we also examined a mutant strain of *E. coli* that shows only tumbling. Below, we shall refer to the wild-type *E. coli* as a swimmer and the mutant *E. coli* as a tumbler. While spiral-like cracks were found in the dried deposits of tumblers and dead swimmers, we observed circular cracks in the dried deposits of swimmers. Using the elastic fracture mechanics and the poroelastic theory, we showed that the circular cracks form due to the tensile nature of the radial drying stress once the

[a] Department of Chemical Engineering and Materials Science, University of Minnesota, Minneapolis, MN 55455, USA. E-mail: iamxlma@gmail.com, xcheng@umn.edu

[b] College of Life Science and Technology, Guangxi University, Nanning 530004, Guangxi, China

[c] Department of Physics & Astronomy, University of Wyoming, Laramie, WY 82071, USA

cracks are initiated by the local order structure induced by the collective swimming of wild-type *E. coli*. In contrast, the spiral-like cracks arise from a dynamic interplay between the cracking and delamination of the drying films of immotile bacteria. Our study unambiguously demonstrates the crucial effect of bacterial swimming on the mechanical instabilities of consolidating bacterial films and illustrates the unique features of active matter in infamously complicated drying processes. Our results are also helpful for deciphering different desiccation crack patterns of the dried bacterial films encountered in natural and engineering processes.

2 Experiment

We used two different *E. coli* strains with distinct swimming behaviors in our experiments, *i.e.*, a wild-type strain of swimmers (BW25113) and a mutant strain of tumblers (RP1616). The two strains share a similar body geometry, which has an average length of 3–4 μm and an average width of 0.8 μm (Fig. 1a and d). The culturing protocols of the two strains are detailed elsewhere.[4,5] In addition, we have also studied the drying behaviors of the suspensions of dead swimmers. The dead bacteria were obtained from the suspensions of active wild-type swimmers sitting in sealed micro-centrifuge tubes for at least four days. The bacteria were confirmed to be immotile from direct optical microscopy. To avoid any potential complication due to the change of the buffer quality over the long waiting, we washed the dead bacteria and resuspended them in DI water at a targeted concentration before each experiment.

In a typical experiment, we prepared a suspension of bacteria with an initial volume fraction ϕ_i of 10–20%. A microscopic glass slide cleaned with DI water and dried using a blowgun was used as the substrate, which was hydrophilic with

a water contact angle of $\approx 25°$. A drop of the suspension with an initial volume V_i of 2–3 μL was gently deposited onto the substrate for drying. A bright-field inverted microscope was used to image the drying process at a frame rate of 1–20 fps. All experiments were performed at a room temperature of 20 ± 2 °C with a relative humidity of RH = 30 ± 4%. We used a scanning electron microscope (SEM) to image the microstructures of dried bacterial deposits, and an optical non-contact profilometer to measure the temporal evolution of the height profiles of drying bacterial films.

3 Results

3.1 Circular cracks of wild-type swimming bacteria

We observed circular cracks in the dried deposits of suspensions of wild-type swimmers (Fig. 1b and c). Fig. 2a–f show the snapshots of different stages during the formation of circular cracks by drying a drop of a swimmer suspension with V_i = 2.5 μL and ϕ_i = 13%. After the drop was deposited on the substrate (Fig. 2a), evaporation initially occurred predominantly near the pinned contact line of the drop, driving the formation of a compaction front where the concentration of bacteria increased drastically from ϕ_i in the bulk fluid to that close to the random close packing in the consolidating film ϕ. The compaction front displayed an approximately constant length L (Fig. 2g), and continuously moved toward the center of the drop over a time interval of 414 s (Fig. 2b and Video S1 in the ESI†). After the passing of the compaction front, the bacterial film was wet and gel-like and continued to undergo evaporation along the top surface of the film, leading to the accumulation of stress. Once the critical material strength was reached around 427 s, cracks were initiated near the edge of the film to release the excess stress[34] (Fig. 2c and h), which then propagated along a circular path (Fig. 2d and e) over a short interval of about 73 s in a stick-slip fashion and eventually
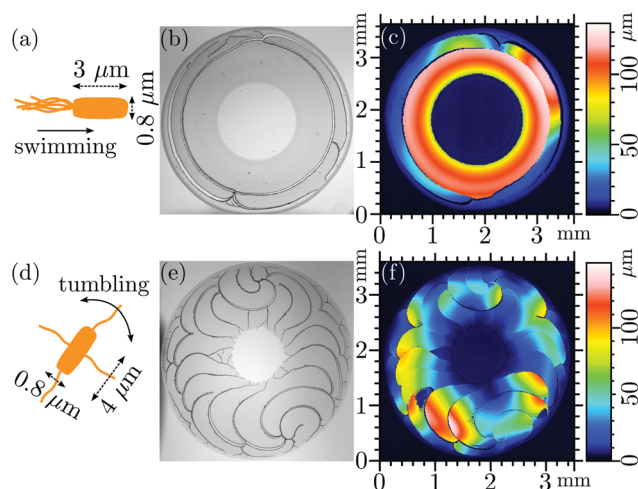

Fig. 1 Schematics of a wild-type *E. coli* with run-and-tumble motion (a) and a mutant *E. coli* with tumbling motion only (d). Bright-field images of the dried deposits of a drop of the wild-type swimmer suspension (b) and a drop of the mutant tumbler suspension (e). Drop volume V_i = 2.5 μL. Bacterial volume fraction ϕ_i = 14%. The corresponding height profiles of the deposits are shown in (c) for swimmers and in (f) for tumblers.
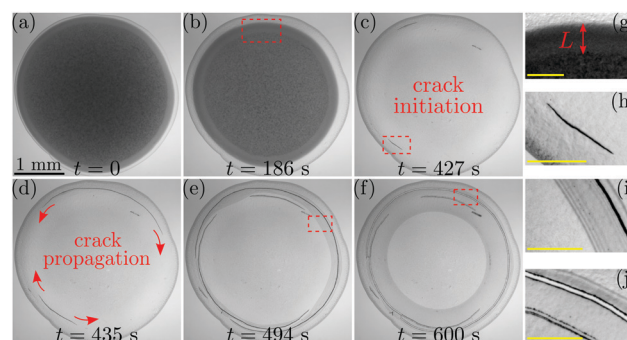

Fig. 2 Snapshots (a)–(f) show the characteristic stages during the formation of circular cracks by drying a drop of the wild-type swimmers with V_i = 2.5 μL and ϕ_i = 14%. The drying process lasted about 10 min before the film completely dried. Image (g) shows the zoom-in view of the red boxed area in (b), where L indicates the width of the compaction front. Image (h) shows the zoom-in view of the first initiated crack in the boxed region in (c). Images (i) and (j) show the zoom-in views of regions near cracks in the boxes in (e) and (f), respectively. Scale bars in (g)–(j) are 250 μm. Video S1 in the ESI† shows the complete drying process corresponding to (a)–(f).

formed the circular cracks (Fig. 2f). Accompanying the crack propagation, the film also delaminated radially toward the center of the drop as indicated by interference fringes in Fig. 2i and j.

To interpret the circular cracks of wild-type swimmers, we calculate the stress distributions in the consolidating bacterial film. Fig. 3a illustrates the geometry of a consolidating film in a cylindrical coordinate. Drying stress was accumulated in the film behind the compaction front in response to the continuously decreasing local liquid pore pressure P_{pore} over time. As evaporation proceeded, the film became flat and thin and evaporation predominantly occurred at the top surface of the film in the late stage of drying. Therefore, P_{pore} satisfies a one-dimensional diffusion equation with $z = 0$ defined at the top surface of the film as follows:[35,36]

$$\frac{\partial P_{pore}}{\partial t} = \frac{\kappa E}{\eta} \frac{\partial^2 P_{pore}}{\partial z^2}, \tag{1}$$

where $\eta \approx 10^{-3}$ Pa s is the dynamic viscosity of water and E is the Young's modulus of the dehydrated film on a glass substrate. We estimated $E \sim 100$ MPa based on our direct measurement using atomic force microscopy, which is consistent with the reported modulus of an isolated dehydrated bacterium.[37] Although the Young's moduli of isolated bacteria and bacterial films are of the same order of magnitude at the microscopic scales, the latter is generally larger depending on the substrate stiffness, humidity, bacterial type and even the fitting model.[38–41] Here, κ is the permeability of the film, which is given by the Carman–Kozeny relationship $\kappa = \frac{1}{45} \frac{(1-\phi)^3}{\phi^2} a^2 \sim 10^{-15}$ m^2, $\phi \approx 0.7$ is the packing fraction of bacteria (Appendix C) and $a \approx 1$ μm is the characteristic size of bacteria. The initial condition is $P_{pore}(z, 0) = P_{atm}$, where $P_{atm} = 10^5$ Pa is the atmospheric pressure. The boundary condition is $\partial P_{pore}/\partial z|_{z=0} = -\eta V_E/\kappa$, where V_E is the steady surface evaporation rate. The evaporation rate is expressed as $V_E = \frac{D_w n_{wsat}}{R} \frac{}{n_w} A(\theta)(1 - RH)$,[42] where $D_w = 25 \times 10^{-6}$ m^2 s is the diffusion coefficient of water into air at room temperature, $R \approx 2$ mm is the drop radius pinned at the contact line, $n_{wsat} = 0.02$ kg m^{-3} is the water density in the vapor at the air–water

interface, $n_w = 1 \times 10^3$ kg m^{-3} is the water density in the bulk liquid, $A(\theta) \approx 1.3$ for a contact angle of $\theta \approx 25°$, and the relative humidity is RH $\approx 30\%$. Therefore, V_E is $\sim 5 \times 10^{-7}$ m s^{-1}. Solving eqn (1), we have P_{pore} given by[43]

$$P_{pore}(z, t) = P_{atm} - P^*(z, t), \tag{2}$$

where

$$P^*(z, t) = \frac{2\eta V_E}{\kappa}\left[\sqrt{\frac{ct}{\pi}}\, e^{\frac{-z^2}{4ct}} + \frac{z}{2}\, \text{erfc}\left(\frac{-z}{\sqrt{4ct}}\right)\right] \tag{3}$$

represents the deviation of the pore pressure from the atmospheric pressure. Here, $c \equiv E\kappa/\eta$ is a constant.

During consolidation, a film is constricted by the substrate; thus the out-of-plane strain ε_{zz} is significantly larger than the in-plane strain $\varepsilon_{rr} + \varepsilon_{\theta\theta}$ driven by shrinkage. Fig. 3b shows the temporal variation of the height profile $h(r)$ along a diameter of a consolidating film from 10 min to 19 min, during which a circular crack forms as indicated by the sharp drop of h at $r \approx 1.4$ mm. The film thickness h decreases significantly during this period, whereas the in-plane contraction is negligible, suggesting that $\varepsilon_{zz} \gg \varepsilon_{rr} + \varepsilon_{\theta\theta}$. Furthermore, since the top surface of the film is traction-free, the deformation of the thin film is predominantly driven by the in-plane stress, suggesting $\sigma_{zz} \ll \sigma_{rr} + \sigma_{\theta\theta}$.[36,42] The same strain and stress conditions have also been applied in modeling the drying of colloidal suspensions on rigid glass substrates.[28]

The in-plane stress components σ_{rr} and $\sigma_{\theta\theta}$ responsible for crack formation are correlated with the equilibrium condition of the stress field in the cylindrical coordinate:

$$\frac{\partial \sigma_{rr}}{\partial r} + \frac{1}{r}(\sigma_{rr} - \sigma_{\theta\theta}) = 0. \tag{4}$$

Using the Biot constitutive relationship of homogeneous and isotropic solids[35] under approximations of $\varepsilon_{zz} \gg \varepsilon_{rr} + \varepsilon_{\theta\theta}$ and $\sigma_{zz} \ll \sigma_{rr} + \sigma_{\theta\theta}$, we have (eqn (A3) in Appendix A):

$$\sigma_{rr} + \sigma_{\theta\theta} = \frac{2P^*(1 - 2\nu)}{1 - \nu}, \tag{5}$$

where ν is Poisson's ratio of the bacterial film. Given the boundary condition $\sigma_{rr}|_{r=R} = P^*$, σ_{rr} and $\sigma_{\theta\theta}$ can be analytically
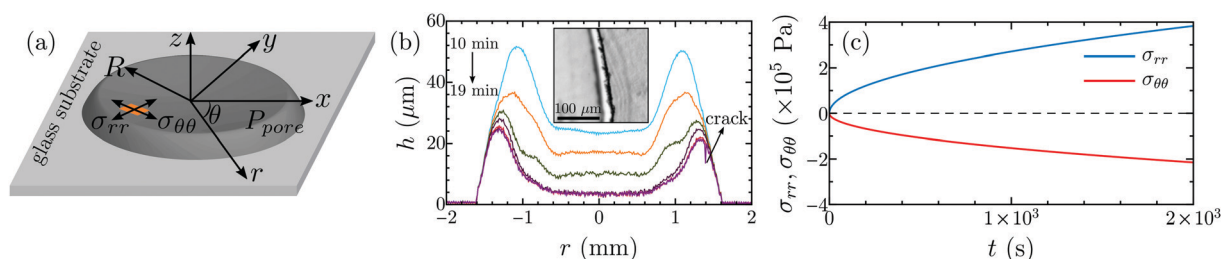

Fig. 3 (a) Illustration of the geometry of a drying drop. (b) The temporal variation of the height profile h of a drying wild-type swimmer drop ($V_i = 2.5$ μL and $\phi_i = 14\%$) along its diameter from $t = 10$ min to $t = 19$ min during which a circular crack forms. The inset shows the segment of the circular crack at $r \approx 1.4$ mm near the scanned region. (c) In-plane stress components σ_{rr} and $\sigma_{\theta\theta}$ from eqn (6) and (7) as a function of t at $r^* = 0.75R$, where $R = 2$ mm is the radius of the drying drop.

solved with eqn (4) and (5) (eqn (A6) and (A7) in Appendix A):

$$\sigma_{rr} = \langle P^* \rangle \frac{r^2(2\nu - 1) - R^2\nu}{r^2(\nu - 1)}, \qquad (6)$$

$$\sigma_{\theta\theta} = \langle P^* \rangle \frac{r^2(2\nu - 1) + R^2\nu}{r^2(\nu - 1)}, \qquad (7)$$

where $\langle P^* \rangle$ the film-thickness-averaged liquid pressure (eqn (A5) in Appendix A).

It has been shown that biofilms including those of *E. coli* behave mechanically similar to polymeric materials, which have Poisson's ratios ν ranging between 0.4 and 0.5. The range has been adopted in many previous experimental, numerical and theoretical studies on biofilms.[38,44–50] Here, we took the lower bound of $\nu = 0.4$ to accommodate the condition that the bacteria film was still undergoing drying at the point of cracking. Choosing any value between 0.4 and 0.5 would not qualitatively change our results. With $R \approx 2$ mm and $h \approx 20$ μm (the thickness of the film at which the crack is generated, see Fig. 3b), eqn (6) and (7) predict the spatiotemporal stress distributions within the drying film.

Fig. 3c shows $\sigma_{rr}(r^*, t)$ and $\sigma_{\theta\theta}(r^*, t)$ at a fixed location $r^* = 0.75R$ where the cracks formed in the experiment. Note that σ_{rr} is tensile ($\sigma_{rr} > 0$) and reaches $\sigma_c \sim 10^5$ Pa when $t > 200$ s, suggesting the formation of the cracks in the circumferential direction at large times. Here, σ_c is the critical stress for cracking, which can be estimated based on the critical film thickness at which cracks form (Appendix B). In comparison, $\sigma_{\theta\theta}$ is compressive ($\sigma_{\theta\theta} < 0$), precluding the formation of cracks in the radial direction that are commonly observed in the drying films of colloidal suspensions[42,51] based on the principle of fracture mechanics. Note that for drying the colloidal suspensions with a typical Poisson's ratio of $\nu = 0.2$,[52–55] $\sigma_{\theta\theta} > 0$ is tensile, which allows for the formation of radial cracks.

In addition to changing the mechanical properties of drying bacterial films, the active swimming of bacteria also modifies the microscopic structure of the consolidating bacterial films, which further facilitates the formation of circular cracks. Fig. 4a shows the two-dimensional (2D) flow field of a suspension of wild-type swimmers near the compaction front during drying, which exhibits the characteristic swarming vortices induced by

bacterial collective swimming.[4,5] Such a coherent dynamic structure was preserved throughout the drying course and gave rise to the local order packing of bacteria in the dried deposit as indicated by the red arrows in Fig. 4b. The circular crack marked by the yellow arrows propagated through this local order structure.

It has already been shown that drying cracks prefer to propagate along the order direction of underlying microstructures due to the least resistance to release stress during crack propagation.[27] In the simple case of drying suspensions of colloidal ellipsoids where the ellipsoids align parallel to the contact line of drying films, the effect leads to the formation of circular cracks along the circumference of dried annular deposits.[27] In a drying bacterial film, although the swarming vortices do not align along the circumference of the drying film, the order structure should still act locally as a nucleation point, promoting the formation of the initial crack at small bacterial scales. As swarming vortices are mesoscopic on the order of a few tens of microns, the structure of the drying film at large scales is still isotropic. Thus, upon nucleation and after the size of the initial crack reaches the scale of a single swarming vortex, the drying film can be treated as a homogeneous medium with isotropic mechanical properties for the propagation of cracks at large scales. The radial tensile stress calculated in our simple homogeneous model (eqn (6)) should then be valid, which directs the propagation of cracks and eventually leads to the formation of circular cracks in the dried deposit.

Finally, Fig. 2i and j show that along with the propagation of the circular cracks, the film also delaminated toward the center of the drying drop. Owing to the strong humidity gradient across the film thickness during drying,[56] the in-plane tensile stress σ_{rr} is localized near the top surface of the film, which gives rise to a stress gradient across the film as illustrated in Fig. 5. Such a stress gradient creates a bending moment M, promoting the film delamination from the edge of the drop to the center of the drop once the accumulated stress is beyond the critical stress for delamination.[43,56,57] We estimated both the critical stress for cracking σ_c and the critical stress for delamination σ_d (Appendix B), which are of the same order of magnitude of $\sim 10^5$ Pa. Hence, immediately following the formation of the circular cracks, the film delaminated from
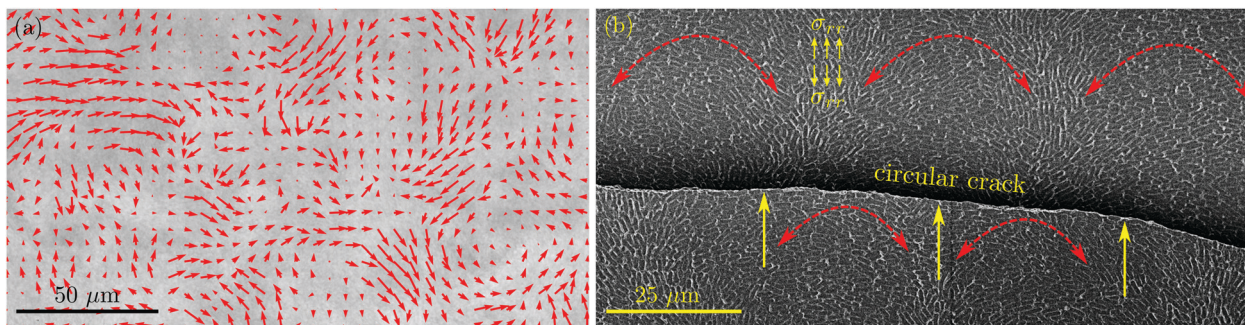

Fig. 4 (a) Snapshot of the 2D flow field of a swimmer suspension near the compaction front during drying. (b) SEM image of the local order structure (red arrows) near a segment of a circular crack (yellow arrows) in a dried swimmer deposit. Video S2 in the ESI† shows the 2D flow field of the drying swimmer suspension corresponding to (a).
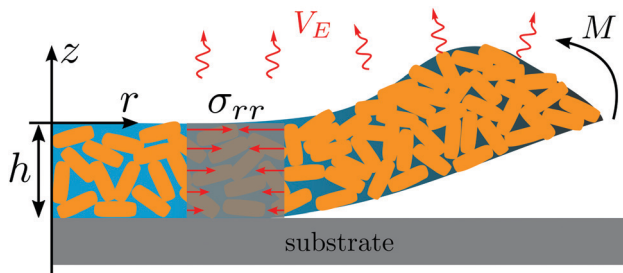
Fig. 5 Schematic illustration of the delamination of a consolidating swimmer film in the radial direction driven by the gradient of the tensile stress σ_{rr} across the film thickness.

the new crack surface toward the center of the drying drop. Fig. 1c shows the height profile of a completely dried swimmer film, which quantitatively illustrates the extent of film delamination. The part of the film close to the inner edge has a height of over 90 μm above the substrate (the red color), while the thickness of the bacterial film near the pinned contact line (the blue color) and in the final stage of the drying process before delamination (Fig. 3b) is less than 30 μm.

3.2 Spiral-like cracks of immotile bacteria

To verify the role of active swimming in the formation of circular cracks, we further examined the crack patterns of mutant tumblers and dead swimmers. Neither of the two types of bacteria showed the collective swimming in drying drops. In contrast to the circular cracks of wild-type swimmers, we observed spiral-like cracks in the dried deposits of these two types of immotile bacteria as shown in Fig. 1d–f and 6.

Fig. 7a–f show the snapshots of different stages during the formation of the spiral-like cracks by drying a drop of a tumbler suspension with V_i = 2.5 μL and ϕ_i = 14%. The compaction front of the drying tumbler suspension was significantly wider than that of the drying swimmer suspension (Fig. 2) and increased in width over time (comparing Videos S1 and S3 in the ESI†). As the accumulated stress reached the material strength, hairpin-shaped cracks facing the center of the drying film first appeared (boxed regions in Fig. 7c and d), which simultaneously initiated the delamination of the film between the two arms of the hairpins (interference fringes in Fig. 7h and i). Upon the creation of new surfaces by cracking, the film subsequently delaminated perpendicularly to and outside the arms of the
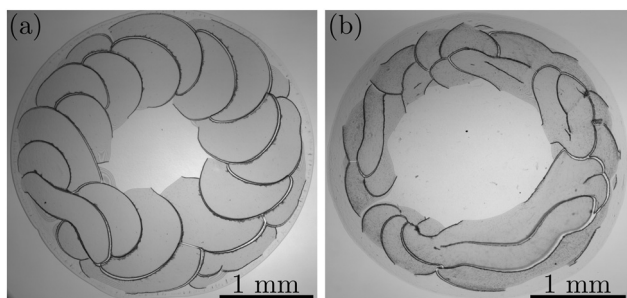

Fig. 6 Bright-field images of the dried deposits of drops of mutant tumblers (a) and dead wild-type swimmers (b) with V_i = 2.5 μL and ϕ_i = 14%.

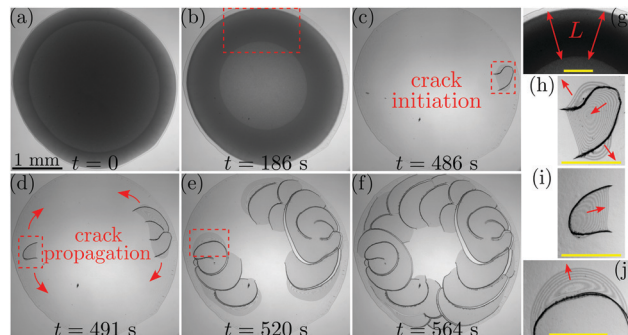Fig. 7 Snapshots (a)–(f) show the characteristic stages during the formation of spiral-like cracks by drying a tumbler drop with V_i = 2.5 μL and ϕ_i = 14%. The drying process lasted about 10 min before the film completely dried. Image (g) shows the zoom-in view of the red boxed area in (b), where L indicates the width of the compaction front. Images (h) and (i) show the first initiated crack in the boxed regions in (c) and (d), respectively. Image (j) shows the boxed area in (e), which displays the propagation of the delamination front along the circumferential direction as indicated by the arrow. The scale bars in (g)–(j) are 400 μm. Video S3 in the ESI† shows the complete drying process corresponding to (a)–(f).

hairpins and propagated along the circumferential direction (Fig. 7h). The delamination front showed an arc shape, which triggered the formation of a crack of the same shape at the front (Fig. 7e and j). The crack in turn created a new surface for further delamination. This cycle of cracking and delamination repeated with time until the cracks initiated by different hairpins met, which ultimately resulted in the spiral-like crack pattern shown in Fig. 7f. Thus, the spiral-like cracks of immotile bacteria stem from the dynamic interplay between film cracking and delamination.

Due to the absence of the collective swimming, tumblers were isotropically distributed in a dried deposit as evidenced in Fig. 8, in contrast to the local order structure in the dried deposit of wild-type swimmers (Fig. 4b). Fig. 1f further shows the height profile of the dried deposit of tumblers. By comparing Fig. 1c and f, one can see that, near the inner drop edge, the degree of the delamination of the deposit of swimmers was much stronger than that of tumblers. The observation indicates that the dried deposit of active swimmers was thicker near the edge than that of immotile tumblers, as the bending moment responsible for film delamination is proportional to the film thickness.[58] Thus, from the conservation of the number of bacteria, the thickness of the deposit of tumblers should be more uniform than that of swimmers. The conclusion is further supported by the direct observation that the extent of the dried deposit of tumblers was larger than that of swimmers (comparing Fig. 1b and e). The more uniform deposit of tumblers likely arose due to the underlying uniform amorphous structure of bacteria with a relatively low packing density. In contrast, swimmers exhibited a local order structure of a high packing density near the pinned contact line, while maintained an amorphous structure of a low packing density near the center.

Our systematic control experiments on the drying suspensions of mutant tumblers and dead wild-type swimmers demonstrate that the local order structure driven by the
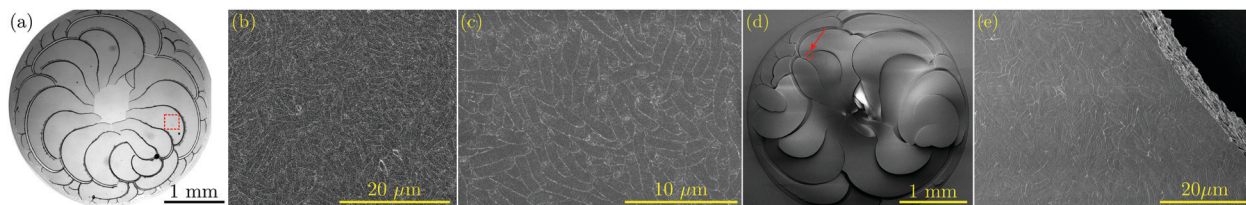
Fig. 8 (a) Bright–field image of a dried tumbler deposit with V_i = 2.5 µL and ϕ_i = 20%. (b) and (c) SEM images of an area away from cracks enclosed by the red box in (a) with different magnifications. (d) SEM image of another dried tumbler deposit with V_i = 2.5 µL and ϕ_i = 20%. (e) The zoom–in view of the area near a spiral–like crack enclosed by the red box as indicated by the red arrow in (d).

collective swimming of wild-type bacteria plays an important role in the formation of circular cracks. More broadly, our experiments show that the crack patterns in the consolidating films of microorganisms can be tuned by manipulating the swimming behaviors of microorganisms.

4 Discussion and conclusions

It is interesting to compare the similarities and differences between the crack patterns of drying bacterial suspensions and drying suspensions of colloidal ellipsoids. First, counterintuitively, the crack pattern of immotile bacteria is different from that of colloidal ellipsoids. In the drying suspensions of colloidal ellipsoids, driven by the hydrodynamic torque of the capillary flow, the ellipsoids align with their major axes parallel to the pinned contact line, which leads to a nematic order structure near the contact line. As cracks propagate preferably along the order direction, this order structure gives rise to circular cracks in the dried deposit.[27] In contrast, immotile bacteria show an amorphous structure in the dried deposit regardless of their relative locations to cracks (Fig. 8). Such an amorphous structure does not support the order-induced crack propagation. Hence, the crack patterns of colloidal ellipsoids and immotile bacteria are qualitatively different. We hypothesize that the amorphous structure of bacterial films arises because of the presence of randomly oriented flagella and pili on the surface of the body of immotile bacteria, which prevent immotile bacteria from packing orderly.

Second, although circular cracks were observed in both the drying suspensions of wild-type swimmers and suspensions of colloidal ellipsoids, the underlying mechanisms are quite different. As discussed in the previous paragraph, the circular cracks of colloidal ellipsoids form due to the nematic order of particles near the pinned contact line.[27] While swimming bacteria do form a local order structure in the form of swarming vortices, the structure does not yield a large-scale system-wide nematic order along the contact line (Fig. 4). Instead, the large-scale circular cracks of drying bacterial films form due to the combined effect of the tensile stress along the radial direction σ_{rr} and the compressive stress along the azimuthal direction $\sigma_{\theta\theta}$, as shown by our simple model.

In conclusion, we investigated the mechanical instabilities of evaporation-driven consolidating dense bacterial suspensions, a model system of active matter. Circular cracks were observed in the consolidating films of wild-type swimming *E. coli*, which were

followed by film delamination along the radial direction toward the center of the drying drop. We showed that the circular cracks are initiated by the local order structure of bacteria, which arises from the collective swimming of bacteria in the drying suspensions. The propagation of the circular cracks at large scales is then determined by the tensile nature of the radial drying stress, which were calculated within the framework of elastic fracture mechanics and poroelastic theory. The tensile radial stress in combination with the humidity gradient across the film thickness also leads to the delamination of the consolidating films upon the creation of the free surface by cracking. Moreover, we also observed spiral-like cracks in the dried deposits of immotile bacteria. Such an intriguing pattern stems from the complex interplay between cracking, delamination, film geometry and anisotropic drying stresses. The detailed mechanism of this complicated process is an open question for future research. It should be noted that our simplified model does not capture all of the factors involved in the complex active system of swimming bacteria, particularly those related to biological properties such as quorum-sensing and the variations of bacterial shapes. We hope our findings and simple analyses in these particular experimental settings can serve as a basis for stimulating more experimental, numerical and theoretical studies on drying active matter in the future.

Taken together, our results elucidate the critical role of the microscopic bacterial activity on the macroscopic mechanical instabilities and pattern formation of consolidating bacterial films. Practically, our study provides insights into diverse biological, environmental and industrial processes associated with drying bacterial suspensions, such as the spreading of pathogens, biofilm formation, painting and coating of biological fluids.

Conflicts of interest

There are no conflicts to declare.

Appendix A: derivation of the in-plane stresses σ_{rr} and $\sigma_{\theta\theta}$

For linearly poroelastic solids, the stress and strain are related by the Biot constitutive equation as follows:[35,59]

$$
\begin{aligned}
\varepsilon_{ij} &= \frac{1+\nu}{E}\sigma_{ij} - \frac{\nu}{E}\sigma_{kk}\delta_{ij} + \frac{\alpha(P_{\text{pore}} - P_{\text{atm}})}{3K}\delta_{ij} \\
&= \frac{1+\nu}{E}\sigma_{ij} - \frac{\nu}{E}\sigma_{kk}\delta_{ij} - \frac{\alpha P^{*}}{3K}\delta_{ij},
\end{aligned}
\tag{A1}
$$

where $\alpha \approx 1$ is the Biot–Willis coefficient,[59] ν and $K = E/3(1 - 2\nu)$ are Poisson's ratio and the bulk modulus of the film, respectively. Here, E is the Young's modulus of the film. $P^* = P^*(z, t)$ is given by eqn (3) in the main text. (i, j) take the values of (r, θ, z) in a cylindrical coordinate system. Accordingly, $\sigma_{kk} = \sigma_{rr} + \sigma_{\theta\theta} + \sigma_{zz}$.

Summing up the three principle strains according to eqn (A1) under the approximations $\varepsilon_{zz} \gg \varepsilon_{rr} + \varepsilon_{\theta\theta}$ and $\sigma_{zz} \ll \sigma_{rr} + \sigma_{\theta\theta}$ explained in the main text leads to

$$\varepsilon_{zz} = \frac{1}{3K}(\sigma_{rr} + \sigma_{\theta\theta}) - \frac{P^*}{K}. \tag{A2}$$

In combination with $\varepsilon_{zz} = -\dfrac{\nu}{E}(\sigma_{rr} + \sigma_{\theta\theta}) - \dfrac{P^*}{3K}$ from eqn (A1), we have

$$\sigma_{\theta\theta} + \sigma_{rr} = \frac{2P^*}{3K\left(\dfrac{1}{3K} + \dfrac{\nu}{E}\right)} = \frac{2P^*(1 - 2\nu)}{1 - \nu}. \tag{A3}$$

Plugging eqn (A3) into eqn (4) in the main text leads to

$$r\frac{\partial \sigma_{rr}}{\partial r} + 2\sigma_{rr} = 2P^*\left(2 + \frac{1}{\nu - 1}\right). \tag{A4}$$

Since P shows small variations across the film thickness, we calculate the film-thickness-averaged liquid pressure to remove the weak z dependence

$$\langle P^* \rangle = \frac{1}{h}\int_{-h}^{0} \left[\frac{2\eta V_E}{\kappa}\sqrt{\frac{E\kappa t}{\pi\eta}}e^{\frac{-z^2}{4E\kappa t/\eta}} - \frac{\eta V_E z}{\kappa}\mathrm{erfc}\left(\frac{-z}{2\sqrt{E\kappa t/\eta}}\right)\right]dz$$

$$= \frac{V_E E t}{h}\left[1 + \frac{he^{\frac{h^2}{4ct}}}{\sqrt{\pi ct}} - \frac{h^2 + 2ct}{2ct}\mathrm{erfc}\left(\frac{h}{2}\sqrt{\frac{1}{ct}}\right)\right], \tag{A5}$$

where $c \equiv E\kappa/\eta$.

The stress boundary condition at $r = R$ is $\sigma \cdot \hat{n}|_{r=R} = \sigma_{rr}|_{r=R} = P_{\mathrm{atm}} - P_{\mathrm{pore}} = P^*$.[23] Applying the condition and replacing P^* with $\langle P^* \rangle$ (eqn (A5)), eqn (A4) can be solved:

$$\sigma_{rr} = \langle P^* \rangle \frac{r^2(2\nu - 1) - R^2\nu}{r^2(\nu - 1)}. \tag{A6}$$

Plugging eqn (A6) into eqn (A5) in the main text yields

$$\sigma_{\theta\theta} = \langle P^* \rangle \frac{r^2(2\nu - 1) + R^2\nu}{r^2(\nu - 1)}. \tag{A7}$$

Appendix B: critical stress for cracking σ_c and delamination σ_d

An evaporation-driven consolidating film is prone to crack to release the excess stress once the accumulated stress is beyond the critical stress σ_c. The value of σ_c can be determined by
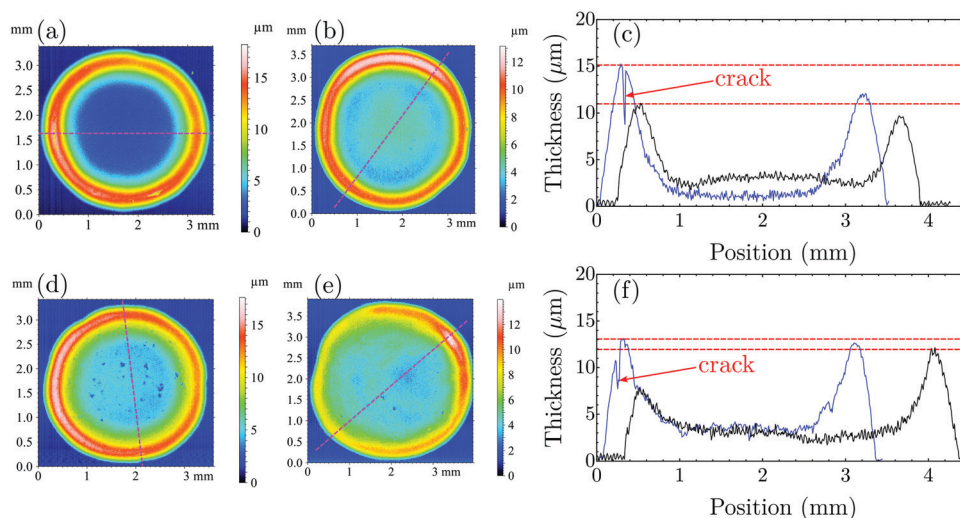

Fig. 9 Height profiles of two dried swimmer deposits (a and b) and two dried tumbler deposits (d and e) with two different film thicknesses. Cracks are present in the thicker films in (a) and (d), but not in the thinner films in (b) and (e). The blue and black curves in (c) and (f) represent the height profiles along the diameters marked by the dashed lines in (a), (b) and (d), (e), respectively. The sharp drops of the blue curves at $r \approx 0.35$ mm in (c) and at $r \approx 0.3$ mm in (f) indicate the presence of cracks. Before delamination at long times, the heights of drying drops are significantly smaller than those shown in Fig. 1c and f.

measuring the corresponding critical film thickness h_c as follows:[60,61]

$$\frac{\sigma_c a}{2\gamma} = 0.1877 \left(\frac{2a}{h_c}\right)^{2/3} \left(\frac{GM_c \phi a}{2\gamma}\right)^{1/3}, \quad \text{(B1)}$$

where $G = \dfrac{E_b}{2(1 + \nu_b)}$ is the shear modulus of bacteria, E_b and ν_b are the Young's modulus and Poisson's ratio of the dehydrated bacteria, a is the characteristic radius, γ is the surface tension, M_c is the coordination number, and ϕ is the 3D packing fraction. To measure h_c, we prepared drops of bacterial suspensions with $V_i = 2.5$ μL and various ϕ_i, and deposited them on glass substrates for drying to obtain the dried deposits of different thicknesses.

Fig. 9 shows the measurements of the height profiles along the diameters of two dried deposits of swimmer drops (Fig. 9a–c) and two dried deposits of tumbler drops (Fig. 9d–f). In both cases, cracks were initiated in the dried deposits with the larger film thickness, but not in the deposits with the smaller film thickness. The critical film thickness for cracking, h_c, should lie between these two thicknesses. We simply took the average of the maximum values of the blue and black curves as indicated by the dashed lines in Fig. 9c and f, which gave the estimate $h_c \approx 13$ μm for swimmers and $h_c \approx 12.5$ μm for tumblers. Plugging the typical values of $E_b = 300$ MPa,[37] $\nu_b = 0.2$[37] $a = 1$ μm, $\gamma = 72$ mN m^{-1}, $M_c = 6$, and $\phi \approx 0.7$ for swimmers or $\phi \approx 0.6$ for tumblers (Appendix C) into eqn (B1), we have the critical stress $\sigma_c \sim 10^5$ Pa for both swimmers and tumblers.

The critical stress for film delamination σ_d can be estimated by[62]

$$\sigma_d = \sqrt{\frac{2E\Gamma_d}{h_d}}, \quad \text{(B2)}$$

where Γ_d is the adhesion strength of the film, E and h_d are the Young's modulus and critical delamination thickness of the film, respectively. Although it is challenging to directly measure the adhesion between an evaporation-driven consolidating bacteria film and a glass substrate, the adhesion strength for most biofilms is of the order of magnitude of 5 mJ m^{-2}.[50,63–67] Here, the Young's modulus of the dehydrated bacteria films can be estimated as $E \sim 100$ MPa. In our experiments, the film delamination and cracking developed nearly simultaneously. Therefore, we simply took $h_d \approx h_c \approx 13$ μm. Plugging the values of Γ_d, E and h_d into eqn (B2) yields $\sigma_d \sim 10^5$ Pa for swimmer films, which is of the same order of magnitude as σ_c. Following the same analysis, σ_d of tumbler films is also the same order of magnitude at $\sim 10^5$ Pa.

Appendix C: estimate of the 3D packing fraction of bacteria in dried deposits

To estimate the 3D packing fraction of bacteria in a dried deposit, we first calculate the relationship between the 3D

packing fraction ϕ and the 2D area fraction ϕ_{2d}. Assuming a cylindrical shape of a bacterial body with a length of l_b and a radius of r_b. The volume of the bacterial body is $V_0 = \pi r_b^2 l_b$ and the cross-sectional area of the body along its major axis is $A_0 = 2r_b l_b$. Consider bacteria within a horizontal layer of length K and width W parallel to the substrate. We assume that all the bacteria are confined within the layer with their major axes aligned parallel to the substrate, a configuration agreeing reasonably well with our SEM images (Fig. 4 and 8). The number of bacteria within the layer is N. The 2D area fraction within the layer is given by $\phi_{2d} = \dfrac{NA_0}{KW} = \dfrac{2Nr_b l_b}{KW}$, whereas the 3D volume fraction is $\phi = \dfrac{NV_0}{KW2r_b} = \dfrac{N\pi r_b l_b}{2KW}$. Thus, $\phi = \dfrac{\pi}{4}\phi_{2d}$. We experimentally measured ϕ_{2d} for wild-type swimmers based on the SEM images (Fig. 4b), which gives $\phi_{2d} \approx 0.96$. Consequently, $\phi \approx 0.75$. We note that the experimental ϕ is slightly larger than the theoretical maximum values of the 3D random packing fraction of rigid cylinders (≈ 0.7),[68–70] which is likely due to the local order structure of bacteria and the approximation taken in our estimate. Similarly, we also measured the 2D area fraction of tumblers in the dried deposit, which gives $\phi_{2d} \approx 0.75$. Thus, the 3D packing fraction of tumblers is $\phi = \dfrac{\pi}{4}\phi_{2d} \approx 0.59$, which is smaller than the 3D packing fraction of the wild-type swimmers as expected.

References

1 V. Schaller, C. Weber, C. Semmrich, E. Frey and A. R. Bausch, *Nature*, 2010, **467**, 73–77.
2 G. Duclos, *et al.*, *Science*, 2020, **367**, 1120–1124.
3 S. Guo, D. Samanta, Y. Peng, X. Xu and X. Cheng, *Proc. Natl. Acad. Sci. U. S. A.*, 2018, **115**, 7212–7217.
4 Y. Peng, Z. Liu and X. Cheng, *Sci. Adv.*, 2021, **7**, eabd1240.
5 Z. Liu, W. Zeng, X. Ma and X. Cheng, *Soft Matter*, 2021, **17**, 10806–10817.
6 J. Palacci, S. Sacanna, A. P. Steinberg, D. J. Pine and P. M. Chaikin, *Science*, 2013, **339**, 936–940.
7 A. Bricard, J.-B. Caussin, N. Desreumaux, O. Dauchot and D. Bartolo, *Nature*, 2013, **503**, 95–98.
8 H. Karani, G. E. Pradillo and P. M. Vlahovska, *Phys. Rev. Lett.*, 2019, **123**, 208002.
9 S. Ramaswamy, *Annu. Rev. Condens. Matter Phys.*, 2010, **1**, 323–345.

10 M. C. Marchetti, J.-F. Joanny, S. Ramaswamy, T. B. Liverpool, J. Prost, M. Rao and R. A. Simha, *Rev. Mod. Phys.*, 2013, **85**, 1143–1189.

11 G. Gompper, *et al.*, *J. Phys.: Condens. Matter*, 2020, **32**, 193001.

12 D. Saintillan and M. Shelley, in *Complex Fluids in Biological Systems*, ed. S. Spagnolie, Springer-Verlag, New York, 2015, pp. 319–355.

13 R. Alert, J. Casademunt and J.-F. Joanny, *Annu. Rev. Condens. Matter Phys.*, 2022, **13**, 143–170.

14 A. K. Epstein, T.-S. Wong, R. A. Belisle, E. M. Boggs and J. Aizenberg, *Proc. Natl. Acad. Sci. U. S. A.*, 2012, **109**, 13182–13187.

15 L. Hall-Stoodley, J. W. Costerton and P. Stoodley, *Nat. Rev. Microbiol.*, 2004, **2**, 95–108.

16 C. G. Kumar and S. K. Anand, *Int. J. Food Microbiol.*, 1998, **42**, 9–27.

17 D. Yanni, A. Kalziqi, J. Thomas, S. L. Ng, S. Vivek, W. C. Ratcliff, B. K. Hammer and P. J. Yunker, arXiv: 1707.03472, 2017.

18 T. T. Nellimoottil, P. N. Rao, S. S. Ghosh and A. Chattopadhyay, *Langmuir*, 2007, **23**, 8655–8658.

19 W. Sempels, R. De Dier, H. Mizuno, J. Hofkens and J. Vermant, *Nat. Commun.*, 2013, **4**, 1757.

20 T. Andac, P. Weigmann, S. K. Velu, E. Pinçe, G. Volpe, G. Volpe and A. Callegari, *Soft Matter*, 2019, **15**, 1488–1496.

21 T. Kasyap, D. L. Koch and M. Wu, *Phys. Fluids*, 2014, **26**, 111703.

22 A. Agrawal, S. Sinha, R. Mukherjee and D. Mampallil, *Phys. Fluids*, 2020, **32**, 093308.

23 L. Goehring, A. Nakahara, T. Dutta, S. Kitsunezaki and S. Tarafdar, *Desiccation cracks and their patterns: Formation and modelling in science and nature*, John Wiley & Sons, 2015.

24 C. Allain and L. Limat, *Phys. Rev. Lett.*, 1995, **74**, 2981–2984.

25 E. R. Dufresne, E. I. Corwin, N. Greenblatt, J. Ashmore, D. Wang, A. D. Dinsmore, J. Cheng, X. Xie, J. W. Hutchinson and D. A. Weitz, *Phys. Rev. Lett.*, 2003, **91**, 224501.

26 G. Jing and J. Ma, *J. Phys. Chem. B*, 2012, **116**, 6225–6231.

27 V. R. Dugyala, H. Lama, D. K. Satapathy and M. G. Basavaraj, *Sci. Rep.*, 2016, **6**, 30708.

28 H. Lama, T. Gogoi, M. G. Basavaraj, L. Pauchard and D. K. Satapathy, *Phys. Rev. E*, 2021, **103**, 032602.

29 G. Domokos, D. J. Jerolmack, F. Kun and J. Török, *Proc. Natl. Acad. Sci. U. S. A.*, 2020, **117**, 18178–18185.

30 X. Ma, J. Lowensohn and J. C. Burton, *Phys. Rev. E*, 2019, **99**, 012802.

31 A. F. Routh, *Rep. Prog. Phys.*, 2013, **76**, 046603.

32 D. Zang, S. Tarafdar, Y. Y. Tarasevich, M. D. Choudhury and T. Dutta, *Phys. Rep.*, 2019, **804**, 1–56.

33 H. C. Berg, *E. coli in Motion*, Springer Science & Business Media, 2008.

34 A. A. Griffith, *Philos. Trans. R. Soc., A*, 1921, **221**, 163–198.

35 M. A. Biot, *J. Appl. Phys.*, 1941, **12**, 155.

36 F. Giorgiutti-Dauphiné and L. Pauchard, *Eur. Phys. J. E: Soft Matter Biol. Phys.*, 2018, **41**, 32.

37 X. Yao, M. Jericho, D. Pink and T. Beveridge, *J. Bacteriol.*, 1999, **181**, 6865–6875.

38 B. Kundukad, T. Seviour, Y. Liang, S. A. Rice, S. Kjelleberg and P. S. Doyle, *Soft Matter*, 2016, **12**, 5718–5726.

39 C. Even, C. Marlière, J.-M. Ghigo, J.-M. Allain, A. Marcellan and E. Raspaud, *Adv. Colloid Interface Sci.*, 2017, **247**, 573–588.

40 Y. Chen, W. Norde, H. C. van der Mei and H. J. Busscher, *mBio*, 2012, **3**, e00378.

41 Y. Abe, P. Polyakov, S. Skali-Lami and G. Francius, *Biofouling*, 2011, **27**, 739–750.

42 F. Giorgiutti-Dauphiné and L. Pauchard, *Eur. Phys. J. E: Soft Matter Biol. Phys.*, 2014, **37**, 39.

43 R. W. Style, S. S. Peppin and A. C. Cocks, *J. Geophys. Res.: Earth Surf.*, 2011, **116**, F01025.

44 R. K. Robinson, *Encyclopedia of food microbiology*, Academic Press, 2014.

45 C. Laspidou and N. Aravas, *Water Sci. Technol.*, 2007, **55**, 447–453.

46 T. Gan, X. Gong, H. Schönherr and G. Zhang, *Biointerphases*, 2016, **11**, 041005.

47 N. Kandemir, W. Vollmer, N. S. Jakubovics and J. Chen, *Sci. Rep.*, 2018, **8**, 10893.

48 C. Pagnout, B. Sohm, A. Razafitianamaharavo, C. Caillet, M. Offroy, M. Leduc, H. Gendre, S. Jomini, A. Beaussart and P. Bauda, *et al.*, *Sci. Rep.*, 2019, **9**, 9696.

49 A. Rmaile, D. Carugo, L. Capretto, X. Zhang, J. A. Wharton, P. J. Thurner, M. Aspiras, M. Ward and P. Stoodley, *Wear*, 2013, **306**, 276–284.

50 J. Yan, C. Fei, S. Mao, A. Moreau, N. S. Wingreen, A. Košmrlj, H. A. Stone and B. L. Bassler, *eLife*, 2019, **8**, e43920.

51 P. Bourrianne, P. Lilin, G. Sintès, T. Nrca, G. H. McKinley and I. Bischofberger, *Soft Matter*, 2021, **17**, 8832–8837.

52 M. Leang, F. Giorgiutti-Dauphine, L.-T. Lee and L. Pauchard, *Soft Matter*, 2017, **13**, 5802–5808.

53 R. W. Style and S. S. Peppin, *Proc. R. Soc. A*, 2011, **467**, 174–193.

54 A. Badar and M. S. Tirumkudulu, *Soft Matter*, 2022, **18**, 2252–2275.

55 E. Di Giuseppe, A. Davaille, E. Mittelstaedt and M. François, *Rheol. Acta*, 2012, **51**, 451–465.

56 E. Jagla, *Phys. Rev. E: Stat., Nonlinear, Soft Matter Phys.*, 2002, **65**, 046147.

57 Z. Néda, K.-t Leung, L. Józsa and M. Ravasz, *Phys. Rev. Lett.*, 2002, **88**, 095502.

58 F. Giorgiutti-Dauphine and L. Pauchard, *Colloids Surf., A*, 2015, **466**, 203–209.

59 H. F. Wang, *Theory of linear poroelasticity with applications to geomechanics and hydrology*, Princeton University Press, 2017.

60 M. S. Tirumkudulu and W. B. Russel, *Langmuir*, 2005, **21**, 4938–4948.

61 K. B. Singh and M. S. Tirumkudulu, *Phys. Rev. Lett.*, 2007, **98**, 218302.

62 W. Meng, M. Liu, Y. Gan, L. Pauchard and C. Chen, *Eur. Phys. J. E: Soft Matter Biol. Phys.*, 2020, **43**, 64.

63 M. Chen, Z. Zhang and T. Bott, *Biotechnol. Tech.*, 1998, **12**, 875–880.

64 W. Zhang, A. G. Stack and Y. Chen, *Colloids Surf., B*, 2011, **82**, 316–324.

65 V. Dupres, F. D. Menozzi, C. Locht, B. H. Clare, N. L. Abbott, S. Cuenot, C. Bompard, D. Raze and Y. F. Dufrêne, *Nat. Methods*, 2005, **2**, 515–520.

66 Y. Liu, P. A. Pinzón-Arango, A. M. Gallardo-Moreno and T. A. Camesano, *Mol. Nutr. Food Res.*, 2010, **54** 1744–1752.

67 Z. Jiang, T. Nero, S. Mukherjee, R. Olson and J. Yan, *Front. Microbiol.*, 2021, **12**, 1642.

68 A. Donev, F. H. Stillinger, P. Chaikin and S. Torquato, *Phys. Rev. Lett.*, 2004, **92**, 255506.

69 S. Li, J. Zhao, P. Lu and Y. Xie, *Chin. Sci. Bull.*, 2010, **55**, 114–119.

70 L. Liu, Y. Yuan, W. Deng and S. Li, *J. Chem. Phys.*, 2018, **149**, 104503.